

# Clustering of galaxies at 3.6 microns in the Spitzer Wide-area Infrared Extragalactic legacy survey

I. Waddington,<sup>1</sup> S. J. Oliver,<sup>1</sup> T. S. R. Babbedge,<sup>2</sup> F. Fang,<sup>3</sup> D. Farrah,<sup>4</sup>  
A. Franceschini,<sup>5</sup> E. A. Gonzalez-Solares,<sup>6</sup> C. J. Lonsdale,<sup>7,8</sup> G. Rodighiero,<sup>5</sup>  
M. Rowan-Robinson,<sup>2</sup> D. L. Shupe,<sup>3</sup> J. A. Surace,<sup>3</sup> M. Vaccari,<sup>5</sup> C. K. Xu<sup>7</sup>

<sup>1</sup>*Astronomy Centre, University of Sussex, Brighton BN1 9QH, UK*

<sup>2</sup>*Astrophysics Group, Blackett Laboratory, Imperial College London, Prince Consort Road, London SW7 2BW, UK*

<sup>3</sup>*Spitzer Science Center, California Institute of Technology, MS 220-6, Pasadena, CA 91125, USA*

<sup>4</sup>*Department of Astronomy, Cornell University, Space Sciences Building, Ithaca, NY 14853, USA*

<sup>5</sup>*Dipartimento di Astronomia, Universita di Padova, Vicolo Osservatorio 5, I-35122 Padua, Italy*

<sup>6</sup>*Institute of Astronomy, University of Cambridge, Madingley Road, Cambridge CB3 0HA, UK*

<sup>7</sup>*Infrared Processing & Analysis Center, California Institute of Technology, MS 100-22, Pasadena, CA 91125, USA*

<sup>8</sup>*Center for Astrophysics & Space Sciences, University of California San Diego, La Jolla, CA 92093–0424, USA*

Accepted —; Received —; in original form —.

## ABSTRACT

We investigate the clustering of galaxies selected in the 3.6  $\mu\text{m}$  band of the *Spitzer* Wide-area Infrared Extragalactic (SWIRE) legacy survey. The angular two-point correlation function is calculated for eleven samples with flux limits of  $S_{3.6} \geq 4\text{--}400 \mu\text{Jy}$ , over an 8 square degree field. The angular clustering strength is measured at  $> 5\text{-}\sigma$  significance at all flux limits, with amplitudes of  $A = (0.49\text{--}29) \times 10^{-3}$  at one degree, for a power-law model,  $A\theta^{-0.8}$ . We estimate the redshift distributions of the samples using phenomenological models, simulations and photometric redshifts, and so derive the spatial correlation lengths. We compare our results with the GalICS (Galaxies In Cosmological Simulations) models of galaxy evolution and with parameterized models of clustering evolution. The GalICS simulations are consistent with our angular correlation functions, but fail to match the spatial clustering inferred from the phenomenological models or the photometric redshifts. We find that the uncertainties in the redshift distributions of our samples dominate the statistical errors in our estimates of the spatial clustering. At low redshifts (median  $z \leq 0.5$ ) the comoving correlation length is approximately constant,  $r_0 = 6.1 \pm 0.5 h^{-1} \text{ Mpc}$ , and then decreases with increasing redshift to a value of  $2.9 \pm 0.3 h^{-1} \text{ Mpc}$  for the faintest sample, for which the median redshift is  $z \sim 1$ . We suggest that this trend can be attributed to a decrease in the average galaxy and halo mass in the fainter flux-limited samples, corresponding to changes in the relative numbers of early- and late-type galaxies. However, we cannot rule out strong evolution of the correlation length over  $0.5 < z < 1$ .

**Key words:** galaxies: evolution – galaxies: statistics – infrared: galaxies – large-scale structure of universe

## 1 INTRODUCTION

Galaxies are not distributed randomly across the sky. At least at low redshifts, they appear to trace distinct patterns: galaxy clusters are connected to each other by long, filamentary structures of galaxies, interspersed with large voids in which few or no galaxies are seen. A plausible theoretical motivation has arisen for the formation of such large-scale structures (LSS) of galaxies, namely that the galaxies are tracing an underlying distribution of dark matter. In their most modern form, models for the formation of these large scale structures postulate that the evolution of the dark matter den-

sity field is inextricably linked to the formation and evolution of the galaxies themselves (e.g., Cole et al. 2000; Granato et al. 2000; Hatton et al. 2003). These models generally invoke some variation of the biased hierarchical paradigm, in which overdensities, or ‘halos’, in the dark matter distribution undergo successive mergers over time to build halos of increasing mass, with galaxies forming from the baryonic matter in these halos.

From these models, and recent observations, it is clear that the relationship between the properties of galaxies, and the properties of the dark matter halos in which they reside, is subtle, and is an area in which observational constraints are particularly valuable in

constraining models. We would like to know, observationally, what sort of galaxy occupies what sort of halo as a function of redshift, and how the properties of galaxies change with both redshift and the masses of their parent halos. One method that has proven especially useful in providing such observational constraints is measuring clustering amplitudes. Fundamentally, the biased hierarchical paradigm requires that overdensities of dark matter should themselves cluster together on the sky, with the strength of clustering depending on their mass (Kaiser 1984; Bardeen et al. 1986). In principle, we can make great strides in understanding the relationship between galaxies and the underlying dark matter distribution by measuring the clustering strength of galaxies selected in a particular way, and relating this to theoretical predictions for halo clustering (Benson et al. 2001).

Such observations are, however, not straightforward to perform. Reliable clustering measurements require large, homogeneous samples of sources selected over large enough areas of sky to sample a range of dark matter density regimes. Ideally, we would like such observations to be performed in the near- and mid-infrared: the (restframe) near-infrared is most sensitive to evolved stars and so can pick up large samples of passively evolving systems, whereas the mid-infrared is sensitive to the dusty, active sources in which the stars and central black holes in (at least some) passively evolving systems are thought to form. Infrared observatories available up to now, however, have not been capable of mapping large enough areas to the required depths to find sufficient numbers of sources, or in enough bands to even crudely discriminate between different populations.

The launch of the *Spitzer* Space Telescope (Werner et al. 2004) offers the potential to overcome these problems, due to its ability to map large areas of sky in the infrared to greater depths than any previous observatory, and in multiple bands so that dusty, active systems can be differentiated from passively evolving systems. The *Spitzer* Wide-area Infrared Extragalactic (SWIRE) survey (Lonsdale et al. 2003, 2004) is the largest of the *Spitzer* Space Telescope’s six Cycle 1 legacy programmes. The survey covers a total area of 49 square degrees, split between six fields, in all seven of *Spitzer*’s imaging bands (3.6–160  $\mu\text{m}$ ). The area and depth of SWIRE combine to produce a survey of significant comoving volume,  $0.2h^{-3} \text{ Gpc}^3$  over  $0 < z < 2$ , and spatial scales of  $\sim 100h^{-1} \text{ Mpc}$  at  $z \geq 1$ .

A principal goal of SWIRE is to study the clustering behaviour of a variety of extragalactic populations. In Oliver et al. (2004) we presented the first detection of galaxy clustering in the survey, measuring a two-point angular correlation function at 3.6  $\mu\text{m}$  from our validation data, and in Farrah et al. (2006) we presented results on the clustering of Ultraluminous Infrared Galaxies (ULIRGs) at  $z > 1$ . Fang et al. (2004) presented angular correlation functions at 3.6–8.0  $\mu\text{m}$  from the 4-square degree *Spitzer* First Look Survey.

In this paper we extend the analysis of the 3.6- $\mu\text{m}$  clustering to larger scales and fainter flux limits (higher redshifts). We begin with a summary of definitions and formalisms in section 2, then in section 3 we discuss the sample selection, including star/galaxy separation and the angular selection function. In section 4 we present our measurements of the two-point angular correlation function. We compare our results with previous measurements in the K-band (section 5) and with the GalICS semi-analytical simulations (section 6). The angular clustering amplitudes are used to estimate the spatial correlation lengths, which are then compared with simple parameterized models of clustering evolution, the GalICS simulations and results from the literature (section 7). Section 8 draws together some conclusions from our

analysis. We use  $H_0 = 100h^{-1} \text{ km s}^{-1} \text{ Mpc}^{-1}$  with  $\Omega_M = 0.3$  and  $\Omega_\Lambda = 0.7$ . Magnitudes are in the AB system unless otherwise noted.

## 2 DEFINITIONS AND LIMBER’S EQUATION

The spatial two-point correlation function  $\xi(r, z)$  is defined through the joint probability

$$dP(r, z) = N^2[1 + \xi(r, z)]dV_1 dV_2 \quad (1)$$

of finding a galaxy in the volume element  $dV_1$  and a second galaxy in the volume element  $dV_2$  separated by a distance  $r$  at a redshift  $z$ , where  $N(z)$  is the mean number density of sources (e.g., Phillipps et al. 1978). In comoving coordinates, the correlation function can be parameterized as

$$\xi(r, z) = \left(\frac{r}{r_0}\right)^{-\gamma} (1+z)^{\gamma-(3+\epsilon)} \quad (2)$$

where  $r_0$  measures the strength of the clustering at  $z = 0$ ,  $\gamma$  measures the scale-dependence and  $\epsilon$  parameterizes the evolution with redshift (e.g., Phillipps et al. 1978; Overzier et al. 2003).

Several special values of  $\epsilon$  have particular interpretations. (1)  $\epsilon = 0$  is the stable clustering model, where the correlation function is fixed in proper coordinates and clustering grows stronger as the background mass distribution expands with the universe. (2)  $\epsilon = \gamma - 3$  is the comoving case, where clustering remains constant in comoving coordinates and simply expands with the universe. (3)  $\epsilon = \gamma - 1$  is the linear growth model, which corresponds to the application of linear perturbation theory to a scale-free power spectrum in an Einstein-de Sitter universe. We note that these models are qualitative indicators of possible evolution scenarios, rather than realistic clustering models (Moscardini et al. 1998).

The angular two-point correlation function  $w(\theta)$  is a measure of the number of pairs of galaxies with separation  $\theta$  compared with that expected for a random distribution. It is defined through the joint probability

$$dP(\theta) = N_\Omega^2[1 + w(\theta)]d\Omega_1 d\Omega_2 \quad (3)$$

of finding a galaxy in solid angle  $d\Omega_1$  and a second galaxy in solid angle  $d\Omega_2$  separated by an angle  $\theta$ , where  $N_\Omega$  is the mean number density of sources (per steradian) in the survey (e.g., Phillipps et al. 1978). If  $w(\theta)$  is zero, the distribution of galaxies is unclustered.

The angular correlation function,  $w(\theta)$ , is the projection along the line of sight of the spatial correlation function,  $\xi(r, z)$ , and can be calculated from Limber’s equation (Limber 1953; Phillipps et al. 1978). If  $\xi(r, z)$  is parameterized as a power-law, as above, then  $w(\theta)$  is also a power-law

$$w(\theta) = A\theta^{1-\gamma}. \quad (4)$$

The amplitude,  $A$ , of the angular correlation function can be expressed (following, e.g., Efstathiou et al. 1991) as

$$A = \frac{r_0^\gamma f}{c} \frac{\int_0^\infty H(z) (1+z)^{-(2+\epsilon)} D_A^{1-\gamma} (dN/dz)^2 dz}{\left[\int_0^\infty (dN/dz) dz\right]^2} \quad (5)$$

where

$$f = \frac{\sqrt{\pi} \Gamma([\gamma - 1]/2)}{\Gamma(\gamma/2)} \quad (6)$$

with  $\Gamma$  being the standard gamma function. Here,  $dN/dz$  is the redshift distribution,  $D_A$  is the angular diameter distance, and  $H(z)$  is the Hubble parameter,

$$H(z) = H_0 \sqrt{\Omega_M(1+z)^3 + \Omega_k(1+z)^2 + \Omega_\Lambda} \quad (7)$$

(where we have neglected the radiation energy density). The spatial correlation length,  $r_0$ , can thus be calculated from the amplitude of the angular correlation function (eq. 5) if the redshift distribution,  $dN/dz$ , of the sources in the survey is known.

### 3 SAMPLE SELECTION

#### 3.1 *Spitzer* observations

The SWIRE-EN1 field has an area of  $\sim 9 \text{ deg}^2$  and is coincident with one of five fields observed as part of the European Large-Area ISO (Infrared Space Observatory) Survey, ELAIS (Oliver et al. 2000; Rowan-Robinson et al. 2004). The nominal field centre is  $16^{\text{h}} 11^{\text{m}} 00^{\text{s}} +55^\circ 00' 00''$  (J2000). The field was mapped by *Spitzer* at 3.6, 4.5, 5.8 and 8.0  $\mu\text{m}$  with the Infrared Array Camera (IRAC, Fazio et al. 2004) on 2004 January 14–20, and at 24, 70 and 160  $\mu\text{m}$  with the Multiband Imaging Photometer (MIPS, Reike et al. 2004) on 2004 January 21–28 and 2004 July 29. The data can be retrieved from the *Spitzer* archive with a Program Identification (PID) of 185, and the enhanced data products (image mosaics and catalogues) are available from the *Spitzer* Science Center.<sup>1</sup>

Full details of the observations and data processing are given in Surace et al. (2006); here we summarize the essential details. The SWIRE-EN1 field was mapped by IRAC with a large grid of pointings, and at each grid point two 30-second images were taken, each one consisting of multiple dithered exposures. The entire grid was repeated in two epochs, offset by half an array width. Thus, for any point on the sky there are a minimum of four independent sightings (images), and these sightings occur on widely spaced parts of the detector array in order to minimize instrumental signatures. The entire survey has a minimum depth of four coverages, equal to 120 seconds of exposure time. In some areas this can be as high as sixteen coverages, or 480 seconds.

The IRAC data were reduced and flux-calibrated by the *Spitzer* Science Center. Further processing of the individual images removed a number of effects (mostly due to bright objects, primarily stars) that remained in the pipeline products (Surace et al. 2006). The images were then coadded into sixteen large mosaics (or ‘tiles’) of approximately  $0.8 \times 0.8$  square degrees each. Sources were detected and their photometry measured with the SEXTRACTOR package (Bertin & Arnouts 1996). We used the flux measured in a circular aperture of  $3''.8$  diameter, unless the source was significantly extended, in which case we used the flux within the Kron aperture. The source catalogue was a superset of the SWIRE Data Release 2 (Surace et al. 2005), containing fainter objects than published at that time.

#### 3.2 Sample definition

We analyzed eleven flux-limited samples selected at 3.6  $\mu\text{m}$  from the SWIRE-EN1 catalogue (Table 1). The deepest sample contained sources with flux densities  $S_{3.6} \geq 4.0 \mu\text{Jy}$  (or  $m_{36} < 22.4 \text{ mag}$ ), this limit being defined by the flux density at which the differential completeness is approximately 50 per cent. At this level, the integral completeness is 82 per cent (see Fig. 1 and discussion in section 3.3). Flux intervals of  $\Delta \log S_{3.6} = 0.2$  or

**Table 1.** Angular and spatial clustering strengths for each of the samples.  $S_{36}$  are the flux limits,  $A$  are the amplitudes of the angular correlation functions and  $AC$  are the integral constraints.  $\langle z \rangle$  are the median redshifts and  $r_0$  are the spatial correlation lengths, derived from the GalICS redshift distributions for the  $S_{36} = 4.0\text{--}15.9 \mu\text{Jy}$  samples and from the IMPZ redshift distributions for the brighter samples (see section 7).

$S_{36}$ $\mu\text{Jy}$	$A$ $10^{-3}$	$AC$ $10^{-3}$	$\langle z \rangle$	$r_0$ $h^{-1} \text{ Mpc}$
4.0	$0.49 \pm 0.10$	$0.42 \pm 0.09$	1.00	$2.93 \pm 0.34$
6.3	$0.63 \pm 0.14$	$0.54 \pm 0.12$	0.90	$3.18 \pm 0.38$
10.0	$0.98 \pm 0.14$	$0.84 \pm 0.12$	0.80	$3.84 \pm 0.31$
15.9	$1.48 \pm 0.08$	$1.26 \pm 0.07$	0.70	$4.48 \pm 0.14$
25.2	$1.90 \pm 0.17$	$1.63 \pm 0.15$	0.65	$4.78 \pm 0.24$
40.0	$2.47 \pm 0.35$	$2.12 \pm 0.30$	0.60	$5.28 \pm 0.41$
63.4	$4.73 \pm 0.19$	$4.09 \pm 0.17$	0.50	$6.70 \pm 0.15$
100.5	$7.40 \pm 0.29$	$6.39 \pm 0.25$	0.38	$6.47 \pm 0.14$
159.2	$11.31 \pm 0.93$	$9.77 \pm 0.81$	0.28	$5.58 \pm 0.25$
252.4	$17.98 \pm 1.90$	$15.54 \pm 1.64$	0.20	$5.59 \pm 0.33$
400.0	$29.12 \pm 2.61$	$25.16 \pm 2.25$	0.17	$6.15 \pm 0.31$

$\Delta m_{36} = 0.5$  were used, corresponding to intervals of  $\Delta z \sim 0.1$  in the median redshift of the samples (see section 7.1).

The flux limit of the brightest sample was set by the need to have at least 1000 sources in order to measure the amplitude of the angular correlation function with more than 3- $\sigma$  significance. This limit on the minimum number of sources was determined empirically, by calculating  $w(\theta)$  for different subsets of the data, varying both the total number of sources and the width of the angular bins in each subset. The brightest sample contained 1501 sources with  $S_{3.6} \geq 400.0 \mu\text{Jy}$  (or  $m_{36} < 17.4 \text{ mag}$ ).

#### 3.3 Angular selection function

In order to calculate clustering statistics, we require an angular selection function that would describe the distribution of sources in the survey if there was no clustering. This takes the form of a mask, where the value of the mask at each position is the relative probability of finding a source at that location on the sky in the absence of clustering. This mask is then used to simulate a random (i.e., unclustered) catalogue of objects (section 4.1). The probability of detecting a source at any given position depends on the completeness of the survey at that point, which is a function of the noise in the image. A noise map was calculated from the coverage map (i.e. a map of the integration time) and the completeness function was found from simulations, as follows.

Coverage maps were generated for each individual mosaic, recording the number of independent images contributing to each pixel, after taking into account the complex dithering pattern and any missing data due to cosmic ray rejection. The combined map for the whole SWIRE-EN1 field was rebinned by a factor of 5 to a pixel scale of 3 arcsec, reducing the size of the map so that it would fit into memory. This rebinning effectively smoothed the coverage map on a scale of 3 arcsec, closely matching the  $3''.8$ -diameter photometric aperture. Pixels with mean coverage less than 2.95 were excluded from the mask (this allowed for up to one of the images in the full coverage areas to be flagged and rejected due to a cosmic ray). The noise in the mosaics scales with the integration time,  $t$ , as  $\sigma \propto 1/\sqrt{t}$  and so varies with coverage (number of coadded images),  $\kappa$ , also as  $\sigma \propto 1/\sqrt{\kappa}$  (Surace et al. 2005). The coverage mask was then used as a proxy for a noise map.

<sup>1</sup> <http://ssc.spitzer.caltech.edu/legacy>

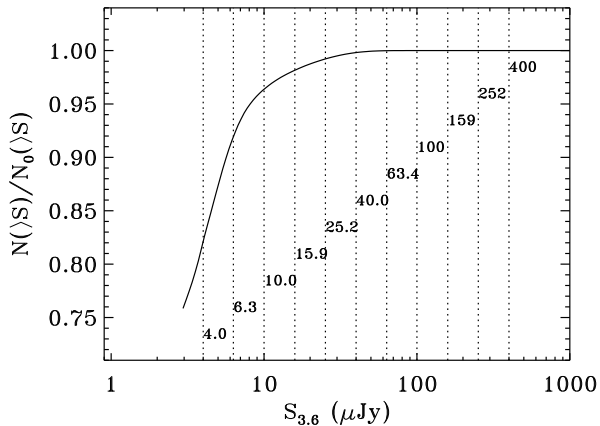


**Figure 1.** The integral completeness function at 3.6  $\mu\text{m}$ .  $N(>S)$  is the cumulative number of sources with fluxes  $\geq S_{3.6}$ , and  $N_0(>S)$  is similarly the cumulative number of sources after correction for incompleteness. The dotted lines show the flux limits of our samples.

We calculated the completeness function by simulating artificial sources and adding them into the SWIRE images. The source extraction stage of the analysis was then repeated, and the new source list was compared with the known positions and fluxes of the artificial sources. The fraction of simulated sources that were recovered by the source extraction was computed as a function of flux and coverage (noise). Fig. 1 shows the integral completeness as a function of flux limit, for an average coverage of 5.0 pointings. The survey is 99% complete at 22  $\mu\text{Jy}$ , 95% complete at 8.1  $\mu\text{Jy}$ , and the integral completeness falls to 82% for our faintest sample at 4.0  $\mu\text{Jy}$ . The simulation results also confirmed that the completeness,  $f$ , scaled as expected with coverage,  $\kappa$ , and flux limit,  $S$ , as  $f(S, \kappa) = f(\sqrt{\kappa}S, 1)$ . At every point in the coverage map, we calculated the integral completeness given the flux limit and coverage. This was then the relative probability that a source in the survey could have been found at that location, in the absence of clustering.

The final contribution to the angular selection function was to exclude circular regions around bright point sources. For this we used the Two-Micron All Sky Survey (2MASS, Skrutskie et al. 2006), masking a circle around all  $K \leq 12$  point sources within a radius,  $R$ , given by  $\log R(\text{arcsec}) = 3.1 - 0.16K$ . This radius was determined by visual inspection of the SWIRE images to find the distance at which the star’s PSF merges into the background. Note that these values are about a factor of two larger than that used in the public SWIRE catalogue (Surace et al. 2005), giving a more conservative mask.

### 3.4 Star/galaxy separation

The presence of stars in the source catalogue artificially dilutes the strength of the galaxy correlations, so it was necessary to remove the stars before performing the clustering analysis. To make the best use of the large survey area, we did not want to be restricted to the limited area with optical coverage, so we developed a procedure to remove stars using only infrared criteria. Our goal was to minimize the number of stars remaining in the sample, but without removing an excessive number of galaxies.

We explored a range of magnitude, colour and stellarity selection criteria in order to identify stars in the infrared data, develop-

ing a three-stage process to remove them. First, the SWIRE catalogue was cross-correlated with the 2MASS survey to classify the bright sources. Objects flagged as being extended in 2MASS are galaxies and bright ( $K \leq 14$  mag) point sources are stars. Second, faint 2MASS sources were classified based on their near- to mid-infrared colours and stellarity at 3.6  $\mu\text{m}$ . Point-like (stellarity  $> 0.94$ ) sources are identified as stars. Sources that are both blue ( $J - m_{36} < -1.50$  or  $H - m_{36} < -2.2$ ) and not clearly resolved (stellarity  $> 0.06$ ) are also stars. Third, stars fainter than 2MASS were classified based on their mid-infrared colours and 3.6  $\mu\text{m}$  stellarity, where blue compact sources are stars. We used three flux bins ( $m_{45} \leq 19.5$ ,  $19.5 < m_{45} \leq 20.0$  and  $20.0 < m_{45} \leq 23.0$ ) with colour cuts of  $m_{36} - m_{45} < -0.35$ ,  $-0.30$  and  $-0.25$ , and stellarity  $> 0.8$ ,  $0.8$  and  $0.7$  respectively to identify stars.

A subset of the SWIRE-EN1 field has optical imaging data which we used to estimate the effectiveness of our infrared star/galaxy separation. The Isaac Newton Telescope Wide Angle Survey (McMahon et al. 2001; Gonzalez-Solares et al. 2004b) observed 6.4  $\text{deg}^2$  of the SWIRE-EN1 survey in five optical bands ( $U, g', r', i', Z$ ) to  $r' \simeq 23.5$  mag. We identified optical counterparts to the SWIRE sources and selected those sources with high optical ( $i$ -band) stellarity according to the SExtractor source extraction software (Bertin & Arnouts 1996). These sources constituted a reference list of stars, against which we compared the infrared classifications. At bright fluxes ( $m_{36} < 21$ ) the stellar contamination in the galaxy sample was estimated to be  $< 3\%$ , rising to 4% at  $m_{36} = 22$ –23. Fainter than  $m_{36} = 23$ , the total star counts are  $\lesssim 3\%$  of the galaxy counts (Fazio et al. 2004) so the contamination is still low, even though we can no longer identify stars at these faint magnitudes. We also compared our galaxy sample with a list of stars identified by the IMPZ photometric redshift estimation code (Babbedge et al. 2004; Rowan-Robinson et al. 2005). Again we found that the stellar contamination in our infrared galaxy catalogue was only 2–4% at  $m_{36} < 23$  mag.

At all fluxes, approximately 10% of the galaxies were rejected by our star selection criteria. There was a slight bias towards rejecting blue (in near- to mid-infrared colours) compact galaxies, but the fraction of galaxies rejected was sufficiently small that this is not expected to significantly bias the measurement of the angular correlation function.

## 4 ANGULAR CORRELATION FUNCTIONS

### 4.1 Method

The angular correlation function (Eq. 4) was estimated by comparing the distribution of galaxies in the survey with catalogues of random sources. The random catalogues were simulated using the angular selection function (Section 3.3), such that the angular distribution of the random sources reflected the geometry and variable depth of the actual survey. We compared each real dataset with 1000 random catalogues, each containing the same number of sources as the galaxy catalogue, ensuring that the uncertainty in the correlation function was not dominated by the scatter between the random catalogues.

A number of methods have been proposed to calculate the angular correlation function; here we use the Landy & Szalay (1993) estimator,

$$\hat{w}(\theta) = \frac{DD - 2DR + RR}{RR} \quad (8)$$

where  $DD$  is the number of galaxy–galaxy pairs at separation

$\theta$ , normalized by the total number of pairs over all separations; and  $DR$  and  $RR$  are similarly the normalized number of galaxy-random and random-random pairs respectively.

The computationally-intensive step in the calculation is counting the number of pairs of sources,  $DD$ ,  $DR$  and  $RR$ . For this we used the NPT pair-counting code of Gray et al. (2004) which uses kd-trees to greatly accelerate the speed of the calculation compared with naive counting methods. We used twelve logarithmically-spaced bins in  $\theta$ , over the range  $0.001 < \theta < 4.0$  degrees, with  $\Delta \log \theta = 0.3$ .

## 4.2 Error estimates and parameter fitting

The large number of sources in the SWIRE dataset allowed us to calculate the errors on the correlation function by comparing subsets of the data. For each of the six faint flux-limited samples (4.0–40.0  $\mu\text{Jy}$ ) we divided the data into 9–25 subsamples of 10,000–15,000 sources each. Two sampling methods were used. First, we randomly selected galaxies across the full field; this gave good statistics on the larger scales ( $> 0.05$  deg). Second, we obtained better statistics on smaller scales by dividing each flux-limited sample into a grid of 9–25 smaller regions and calculating  $w(\theta)$  using all the sources within a sub-region.

For each sub-sampling method, this produced  $n = 9$ –25 independent estimates of the correlation function,  $\hat{w}_i(\theta_j)$ , where  $i$  labels the subsample and  $j$  labels the angular bin. From these  $n$  estimates, we calculated the mean  $\bar{w}(\theta_j) = \sum_{i=1}^n \hat{w}_i(\theta_j)/n$  for each bin. The covariance between angular bins  $\theta_j$  and  $\theta_k$  is given by

$$\sigma_{jk}^2 = \frac{1}{n-1} \sum_{i=1}^n [\hat{w}_i(\theta_j) - \bar{w}(\theta_j)][\hat{w}_i(\theta_k) - \bar{w}(\theta_k)]. \quad (9)$$

As other authors have also found (e.g., Zehavi et al. 2002), the off-diagonal terms become increasingly noisy for elements farther away from the diagonal, making inversion of the covariance matrix unstable, so we only retained the covariances between adjacent bins, i.e. we set  $\sigma_{jk}^2 = 0$  for  $|j - k| > 1$ .

The brighter flux-limited samples (63–400  $\mu\text{Jy}$ ) contained too few sources to divide into independent samples, so to calculate the errors we used the jackknife technique. Each sample was divided into a grid of  $4 \times 4$  sub-areas and we calculated  $\hat{w}_i(\theta_j)$  sixteen times, each time excluding a different sub-area. The best estimate of the correlation function is the mean of the  $\hat{w}_i(\theta_j)$  and the covariance is

$$\sigma_{jk}^2 = \frac{n-1}{n} \sum_{i=1}^n [\hat{w}_i(\theta_j) - \bar{w}(\theta_j)][\hat{w}_i(\theta_k) - \bar{w}(\theta_k)] \quad (10)$$

(Scranton et al. 2002). Again, we only retained the covariances between adjacent bins.

In Fig. 2 we plot the angular correlation functions for the eleven samples, corrected by the integral constraint discussed below. For the faint samples, we show the data from the full-field subsampling, which give the best results on large scales and are consistent on smaller scales with the results of the sub-region sampling.

The angular correlation function is parameterized as a power law  $A\theta^{1-\gamma}$  (Eq. 4), where the amplitude,  $A$ , measures the strength of the clustering, the index,  $\gamma$ , measures its scale-dependence, and  $\theta$  is measured in degrees. Due to the finite size of the survey, the observed  $\bar{w}(\theta)$  is a biased estimator of the real correlation function, and can be modeled as

$$w_m(\theta) = A(\theta^{1-\gamma} - C). \quad (11)$$

The integral constraint,  $AC$ , can be estimated by doubly integrating the (assumed) true  $w_m(\theta)$  over the area of the survey, a calculation that can be done numerically using the random-random pair counts,

$$C = \frac{\sum_j N_{rr}(\theta_j) \theta_j^{1-\gamma}}{\sum_j N_{rr}(\theta_j)} \quad (12)$$

where  $N_{rr}(\theta_j)$  are the unnormalized counts and the summation is over all the angular bins (Roche et al. 1999).

We fitted the model (Eq. 11) to the observed correlation function  $\bar{w}(\theta_j)$  for each of the data samples by minimizing the generalized  $\chi^2$ , defined as

$$\chi^2 = \sum_{j=1}^n \sum_{k=1}^n [w_m(\theta_j) - \bar{w}(\theta_j)] H_{jk} [w_m(\theta_k) - \bar{w}(\theta_k)] \quad (13)$$

where  $H_{jk}$  is the inverse of the covariance matrix,  $(\sigma_{jk}^2)^{-1}$  (Pollo et al. 2005). A wide range of optical and infrared surveys indicate that  $\gamma = 1.8$  and we found that this was consistent with the present data, so fixed  $\gamma$  to this value for comparison with other surveys. The best-fitting models are shown with the data in Fig. 2 and the amplitudes and integral constraints are listed in Table 1.

## 5 COMPARISON WITH K-BAND SURVEYS

The angular correlation function is the projection along the line of sight of the spatial correlation function,  $\xi(r, z)$ , and is dependent on both the redshift distribution and luminosity function of galaxies in the survey and on the evolution of the spatial clustering. At fainter flux limits the survey probes to higher redshifts (larger volumes) and lower luminosities, and both these reduce the strength of the projected clustering. This is shown in Fig. 3 where we plot the amplitude,  $A$ , of the angular correlation function against the limiting magnitude for a range of  $K$ -band surveys. We compare the 3.6- $\mu\text{m}$  SWIRE results with previous  $K$ -band data, due to the abundance of clustering measurements in  $K$  and the relatively few measurements at 3.6- $\mu\text{m}$  (Fang et al. 2004; Oliver et al. 2004). The emission in both the  $K$  and 3.6- $\mu\text{m}$  bands arises from the old stars in a galaxy – both bands are relatively insensitive to the current star formation rate and are good tracers of the stellar mass.

We estimated the equivalent  $K$ -band limit (Vega system) for each of our 3.6  $\mu\text{m}$  selected samples using the average  $K - m_{36}$  colour of SWIRE galaxies detected in the Early Data Release of the UKIRT Infrared Deep Sky Survey (UKIDSS; Dye et al. 2006). We overplot the SWIRE clustering amplitudes on Fig. 3, where the errors in  $K$ -band magnitude correspond to the standard deviation of the  $K - m_{36}$  colour distributions. Our data are consistent with these other surveys, confirming that both bands are selecting similar galaxy populations, with our new results having significantly smaller errors in the amplitudes, due to the much larger survey area at fainter fluxes. The larger area of future UKIDSS data releases will enable us to reduce the uncertainty in the equivalent  $K$ -band limits of SWIRE, particularly at the bright end where there are relatively few sources in UKIDSS at present.

Also plotted in Fig. 3 are three models of clustering evolution (Eq. 2), with  $\epsilon = 0, -0.4$  &  $-1.2$ , from figure 7 of Roche et al. (2003). Following Eq. 5, the amplitude of the angular correlation function can be calculated if the redshift distribution ( $dN/dz$ ) of the survey is known. Roche et al. (2002, 2003) predict the redshift

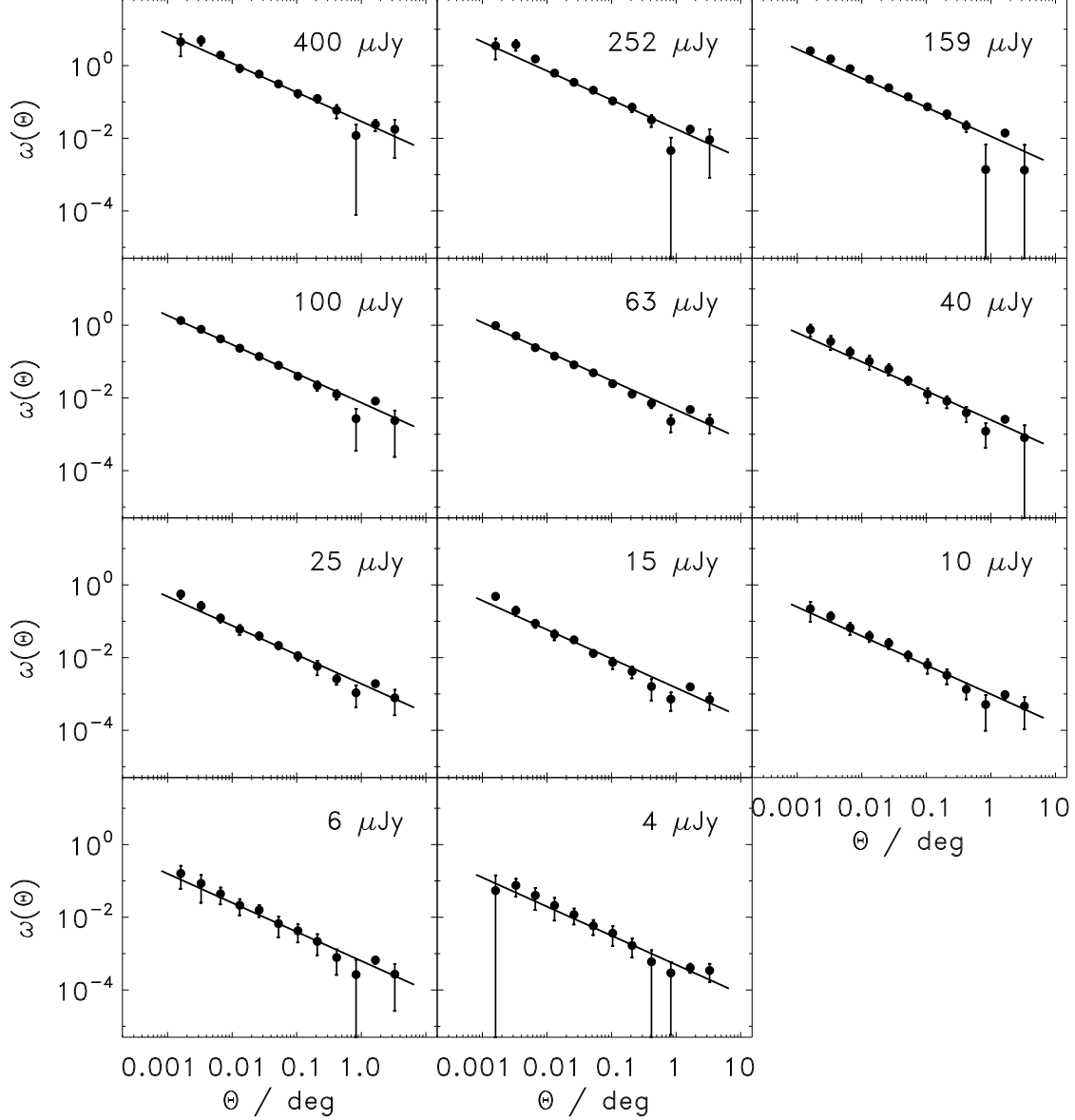


**Figure 2.** Angular correlation functions  $w(\theta)$  for the eleven samples with flux density limits of 4–400  $\mu\text{Jy}$ . Solid lines are the best-fitting power-law model with  $\gamma = 1.8$ , and the data have been corrected for the integral constraint.

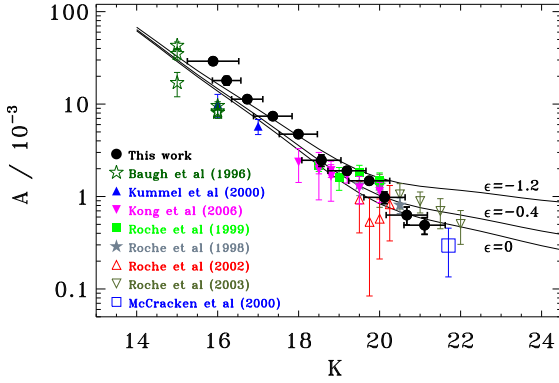
distributions using a simple galaxy evolution model, where they evolve a  $K$ -band galaxy luminosity function according to stellar population synthesis codes, given a star formation history and a galaxy merger rate. We see that the model that best fits the SWIRE data is their stable clustering model ( $\epsilon = 0$ ), with their comoving model ( $\epsilon = -1.2$ ) rejected at  $> 5\text{-}\sigma$  at the faintest magnitudes ( $K \sim 21$ ). We note that these models of the angular clustering are dependent on a range of parameters, not just the evolution of the spatial clustering,  $\epsilon$ , so it is the Roche et al. (2003) merger model with comoving evolution that is a poor fit to the data, and this does not imply that comoving clustering in general can be rejected.

## 6 COMPARISON WITH GALICS MOCK CATALOGUES

GalICS (Galaxies In Cosmological Simulations) is a hybrid model of galaxy evolution which combines high-resolution N-body simulations of the dark matter content of the universe with semi-analytic prescriptions to describe the fate of the baryons within the dark matter halos (Hatton et al. 2003). The simulations have  $256^3$  particles of mass  $8 \times 10^9 M_\odot$ , in a  $100h^{-1}$  Mpc box with a spatial resolution of  $20h^{-1}$  kpc. Within each halo, some fraction of the gas mass is cooled and turned into stars which then evolve. The spectral energy distributions of these model galaxies are computed by sum-

**Table 2.** Spatial correlation lengths,  $r_0$  ( $h^{-1}$  Mpc), and median redshifts,  $\langle z \rangle$ , derived from the SWIRE clustering amplitudes and each of the redshift distributions.  $S_{36}$  are the flux limits in  $\mu\text{Jy}$ .

$S_{36}$	$\langle z \rangle$	Xu et al.		Franceschini et al.		GalICS		IMPZ	
		$r_0$	$\langle z \rangle$	$r_0$	$\langle z \rangle$	$r_0$	$\langle z \rangle$	$r_0$	$\langle z \rangle$
4.0	0.88	$2.85 \pm 0.33$	0.94	$2.95 \pm 0.34$	1.00	$2.93 \pm 0.34$	0.68	$2.46 \pm 0.28$	
6.3	0.84	$3.18 \pm 0.38$	0.88	$3.22 \pm 0.38$	0.90	$3.18 \pm 0.38$	0.68	$2.79 \pm 0.33$	
10.0	0.78	$3.97 \pm 0.32$	0.82	$3.92 \pm 0.32$	0.80	$3.84 \pm 0.31$	0.68	$3.48 \pm 0.28$	
15.9	0.74	$4.82 \pm 0.15$	0.74	$4.66 \pm 0.14$	0.70	$4.48 \pm 0.14$	0.65	$4.25 \pm 0.13$	
25.2	0.70	$5.32 \pm 0.27$	0.68	$5.09 \pm 0.26$	0.60	$4.72 \pm 0.24$	0.65	$4.78 \pm 0.24$	
40.0	0.66	$5.91 \pm 0.46$	0.62	$5.55 \pm 0.43$	0.50	$4.82 \pm 0.37$	0.60	$5.28 \pm 0.41$	
63.4	0.58	$7.70 \pm 0.17$	0.56	$7.33 \pm 0.17$	0.40	$5.78 \pm 0.13$	0.50	$6.70 \pm 0.15$	
100.5	0.46	$8.52 \pm 0.19$	0.48	$8.27 \pm 0.18$	0.30	$5.87 \pm 0.13$	0.38	$6.47 \pm 0.14$	
159.2	0.36	$8.75 \pm 0.40$	0.36	$8.49 \pm 0.39$	0.25	$5.66 \pm 0.26$	0.28	$5.58 \pm 0.25$	
252.4	0.26	$8.58 \pm 0.50$	0.24	$7.97 \pm 0.47$	0.20	$5.61 \pm 0.33$	0.20	$5.59 \pm 0.33$	
400.0	0.20	$8.51 \pm 0.42$	0.18	$7.16 \pm 0.36$	0.15	$5.71 \pm 0.28$	0.17	$6.15 \pm 0.31$	

**Figure 3.** The amplitude,  $A$ , of the angular correlation function, as a function of  $K$ -band limiting magnitude (Vega system), for our SWIRE data (solid circles) and surveys from the literature (Baugh et al. 1996; Kong et al. 2006; Kummel & Wagner 2000; McCracken et al. 2000; Roche et al. 1998, 1999, 2002, 2003). The  $K$ -band limits of the SWIRE data have been estimated from average  $K - m_{36}$  colours (section 5). The lines are models of clustering evolution from Roche et al. (2003).

ming the contribution of all the stars they contain, tracking their age and metallicity. A mock catalogue is generated by projecting a cone through the simulation at a series of timesteps (redshifts), and calculating the properties of the galaxies ‘observed’ in the cone. The GalICS project have made available<sup>2</sup> these 1-deg<sup>2</sup> cones, from which we have extracted mock catalogues of the SWIRE survey.

We calculated the two-point angular correlation functions for the eight GalICS catalogues, each time using the eleven flux-limited samples corresponding to the flux limits listed in Table 1. We used the same method as for the SWIRE data (section 4) and calculated errors and covariances from the eight independent samples. The correlation functions were fitted by a power-law model (Eq. 11) with fixed  $\gamma = 1.8$ , to determine the amplitudes and the integral constraints. The results are given in Table 3.

In Fig. 4 we compare the SWIRE correlation functions (data points) with the GalICS results, where the shaded regions are the one-sigma error bounds from the mock catalogues, and all datasets have been corrected for their integral constraints. At the brightest

**Table 3.** Angular and spatial clustering strengths for the GalICS simulations.  $S_{36}$  are the flux limits,  $A$  are the amplitudes of the angular correlation functions,  $AC$  are the integral constraints,  $\langle z \rangle$  are the median redshifts and  $r_0$  are the spatial correlation lengths.

$S_{36}$ $\mu\text{Jy}$	$A$ $10^{-3}$	$AC$ $10^{-3}$	$\langle z \rangle$	$r_0$ $h^{-1}$ Mpc
4.0	$0.77 \pm 0.03$	$1.56 \pm 0.06$	1.00	$3.76 \pm 0.08$
6.3	$0.87 \pm 0.05$	$1.76 \pm 0.09$	0.90	$3.81 \pm 0.11$
10.0	$1.28 \pm 0.06$	$2.57 \pm 0.12$	0.80	$4.44 \pm 0.11$
15.9	$1.50 \pm 0.13$	$3.03 \pm 0.25$	0.70	$4.53 \pm 0.21$
25.2	$1.87 \pm 0.13$	$3.77 \pm 0.25$	0.60	$4.67 \pm 0.17$
40.0	$2.58 \pm 0.14$	$5.21 \pm 0.27$	0.50	$4.94 \pm 0.14$
63.4	$3.85 \pm 0.42$	$7.76 \pm 0.86$	0.40	$5.15 \pm 0.32$
100.5	$4.18 \pm 0.53$	$8.43 \pm 1.07$	0.30	$4.27 \pm 0.30$
159.2	$10.67 \pm 2.07$	$21.52 \pm 4.18$	0.25	$5.48 \pm 0.59$
252.4	$13.47 \pm 2.42$	$27.16 \pm 4.88$	0.20	$4.78 \pm 0.48$
400.0	$15.92 \pm 4.06$	$32.07 \pm 8.18$	0.15	$4.08 \pm 0.58$

flux limits ( $S_{3.6} \geq 159 \mu\text{Jy}$ ), the large uncertainties in the model correlation functions, particularly on small scales, are due to the small size (1 sq. deg.) of the simulations compared with the data (8.1 sq. deg.). There are less than 1000 sources in each of these bright samples, and it is seen that this is insufficient to measure  $w(\theta)$  accurately at  $\theta \lesssim 0.01$  deg. Similarly, the greater uncertainties in the models on large scales are due to the smaller angular size of the GalICS catalogues. The largest angular scale of the simulations is 1.4 deg compared with 4.1 deg for the data, although the measurement of  $w(\theta)$  becomes uncertain on scales much smaller than the maximum extent of either survey.

We compared the GalICS correlation functions with the SWIRE results using a  $\chi^2$  test. If the two smallest scale bins are excluded from the comparison, then the data and simulations do not differ significantly. Even for the faintest two samples (4 and 6  $\mu\text{Jy}$ ), where the simulations lie consistently above the data in Fig. 4, the difference is not statistically significant. However the small-scale discrepancies between the simulations and the data are worth noting. The GalICS correlation functions deviate from a power law at scales  $\lesssim 30$  arcsec at all flux limits for which there is good data on small scales. The  $\chi^2$  test gives the probability that the data and simulations are drawn from the same distribution as only  $10^{-2}$ – $10^{-4}$  for these small scales, for almost all samples brighter than  $S_{36} \geq 15 \mu\text{Jy}$ .

This lack of close ( $\lesssim 100 h^{-1}$  kpc) pairs in the GalICS

<sup>2</sup> <http://galics.cosmologie.fr/>

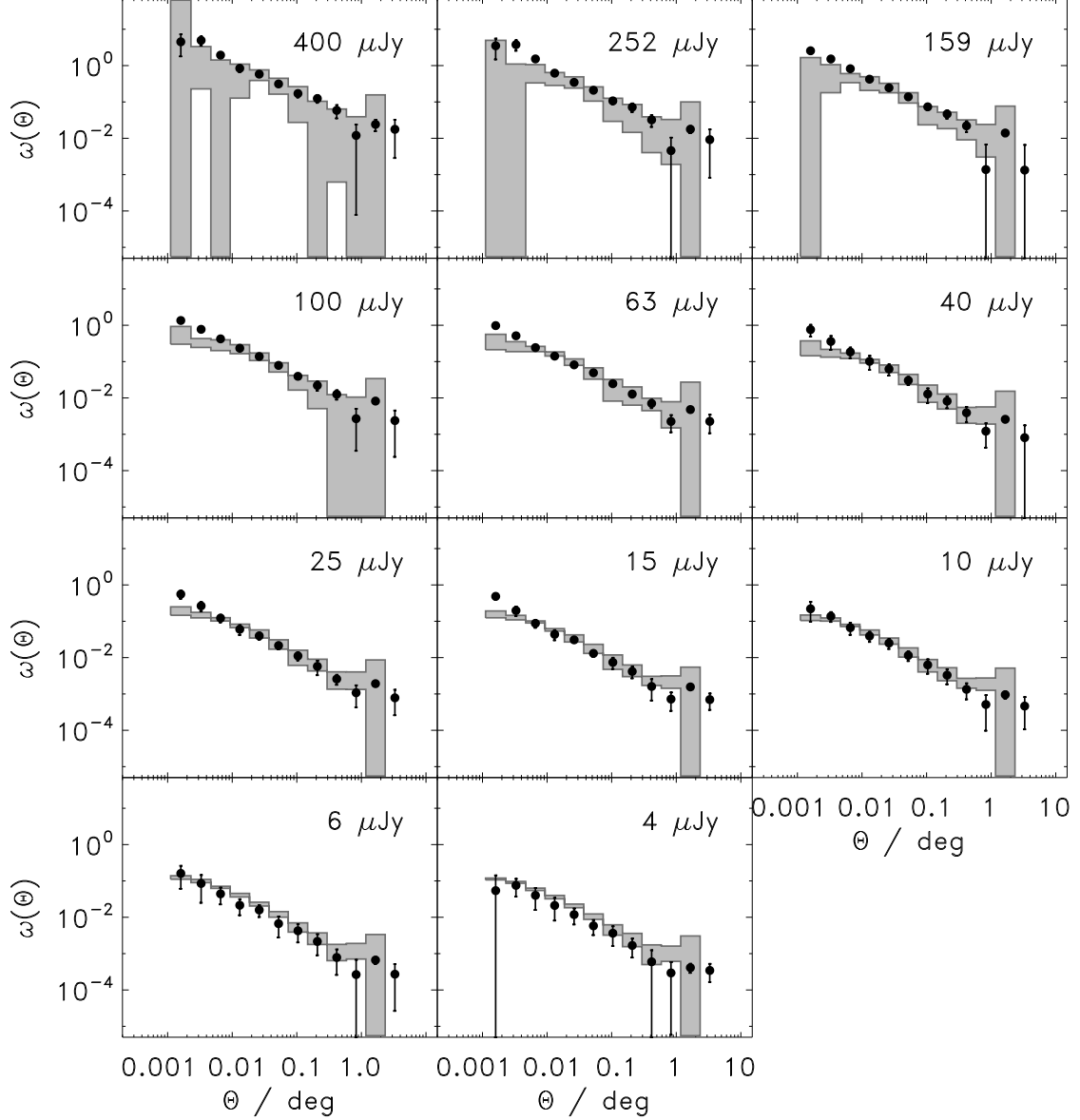


**Figure 4.** Angular correlation functions  $w(\theta)$  for the eleven flux-limited samples compared with the GalICS simulations. The shaded regions are the one-sigma error bounds on  $w(\theta)$  from the mock catalogues; the data points correspond to Fig. 2. Both the data and the simulation results have been corrected for their integral constraints.

simulations, corresponding to the scale of galaxy groups and smaller, was also observed by Blaizot et al. (2006) in their comparison of the GalICS angular correlation functions with those of the Sloan Digital Sky Survey (York et al. 2000). This can be explained within the context of Halo Occupation Distribution models (e.g., Berlind & Weinberg 2002). Such models have shown that the galaxy correlation function can be decomposed into two terms: (i) correlations between galaxies in different halos (large scales), and (ii) correlations between pairs of galaxies located within the same halo (small scales). Blaizot et al. (2006) showed that the GalICS

simulations underestimate this clustering of galaxies within a single halo, and this leads to the turnover of the GalICS correlation function at small scales, as we see in Fig. 4.

There is a second factor which may contribute to the underestimate of small-scale clustering in the simulation results. The galaxy mass resolution limit of GalICS corresponds to a limiting galaxy luminosity ( $M_K < -22.7$  in the restframe  $K$ -band) and an absence of low-mass/low-luminosity galaxies in the simulations would also reduce the number of close pairs. A luminous galaxy is far more likely to have a low-luminosity companion, simply because their



number density is that much greater, and if these low-luminosity galaxies are missing from the simulation, then there will be an absence of close pairs. As discussed below (Section 7), the fainter samples contain proportionately more low-luminosity galaxies than the bright samples, and if these are missing from the GalICS models due to the mass resolution limit, then that could also explain the trend for the models to over-predict the clustering at 4 and 6  $\mu\text{Jy}$ .

Overall, the GalICS simulations are in excellent agreement with the angular clustering of 3.6- $\mu\text{m}$  selected galaxies in SWIRE. However, the failure to resolve low-mass sources and to correctly predict the clustering within a given halo, indicate that these data are pushing the GalICS models to their limit.

## 7 SPATIAL CLUSTERING

### 7.1 Redshift distributions

The angular correlation function is the projection along the line of sight of the spatial correlation function. We have used the inverse of Limber's equation (Eq. 5) to estimate the strength of the spatial clustering, expressed as the correlation length,  $r_0$ , from our measurements of the angular clustering amplitude,  $A$ . Limber's equation is expressed in terms of the redshift distribution of the sample,  $dN/dz$ , which incorporates the radial selection function, i.e. the probability that a source at a given redshift could have been detected in the survey. We have used four independent estimates of the redshift distribution to calculate the spatial correlation lengths for each SWIRE sample.

The first two distributions were those predicted from the phenomenological models of Xu et al. (2003) and Franceschini et al. (2006). These models combine local luminosity functions with parametric modeling of luminosity and/or density evolution to predict the relative numbers of different galaxy populations as a function of redshift. Several populations are defined (for example, early-type, late-type, starburst, AGN), with spectral energy distributions drawn from observed or model template libraries, giving multi-wavelength predictions for the evolution of the galaxy populations. These models fit a wide range of observational data, in particular the mid-infrared number counts from *Spitzer* surveys.

The GalICS simulations (Hatton et al. 2003) provided the third redshift distribution, and the fourth estimate of  $dN/dz$  was based on the SWIRE survey directly, using the IMPZ photometric redshift catalogue (Babbedge et al. 2004; Rowan-Robinson et al. 2005). The redshift distributions are shown in Fig. 5 and their median redshifts are listed in Table 2. The median redshifts are in good agreement with each other for flux limits of  $S_{36} = 25 \mu\text{Jy}$  and brighter, corresponding to median redshifts of  $\langle z \rangle < 0.7$ –0.8. Fainter than this, the model distributions continue to shift to higher redshift with decreasing flux limit, but the median redshift of the observational estimate (IMPZ) remains constant. This primarily reflects the incompleteness of the optical identifications of the SWIRE survey, as the photometric redshift code is driven by the optical data. We find that only 40 per cent of the 4  $\mu\text{Jy}$  sample have photometric redshifts compared with  $> 90$  per cent of sources brighter than 40  $\mu\text{Jy}$ . The sources without redshifts are those that are optically faint and so are more likely to be galaxies at high redshift.

Also plotted in Fig. 5 (shaded histograms) are the redshift distributions of the K20 survey (Cimatti et al. 2002; Mignoli et al. 2005). The K20 survey is a near-infrared ( $K_s < 20$ , Vega system) redshift survey of 545 sources, with a high spectroscopic

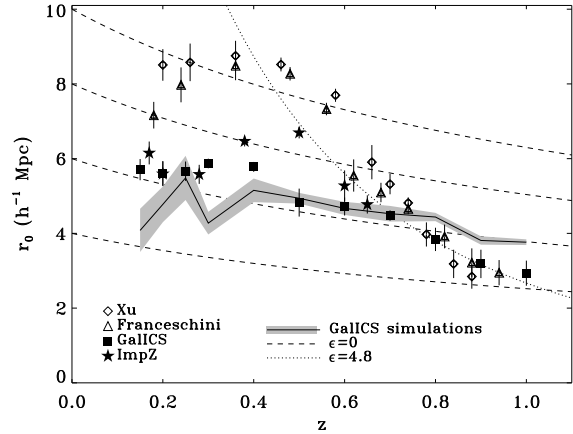


**Figure 6.** The comoving correlation length,  $r_0$ , calculated from the SWIRE clustering amplitudes, as a function of median redshift, derived from each of the redshift distributions: Xu et al. (2003), Franceschini et al. (2006), GalICS (Hatton et al. 2003) and IMPZ (Babbedge et al. 2004). The solid line shows the results derived from the angular clustering measured from the GalICS simulations, with one-sigma error bounds shown in grey. The dashed lines are the stable clustering ( $\epsilon = 0$ ) parametric models for different normalizations at  $z = 0$ . The dotted line is the best-fitting epsilon model at  $z > 0.45$ , with  $\epsilon = 4.8 \pm 0.8$  and  $r_0 = 27 \pm 6 h^{-1} \text{ Mpc}$ .

completeness of 92 per cent. Using the equivalent  $K$ -band flux limits of the SWIRE samples (section 5), we compared our estimates of the SWIRE redshift distributions with the observed K20 data. The spectroscopic redshift distributions are consistent with the SWIRE estimates, however they do not distinguish between the different models or the IMPZ photometric redshifts – there are simply too few sources with spectroscopic redshifts, particularly in the brighter samples. One can also see a peak in the K20 distributions at  $z \simeq 0.7$ , corresponding to a cluster or other large-scale structure in the K20 survey.

This illustrates how the small size of current  $K$ -band selected redshift surveys (typically less than 1000 sources) restricts their usefulness in defining a redshift distribution, due to small-number statistics and cosmic variance. This, together with significant selection biases (typically they target high-redshift or very red sources), makes them unsuitable as redshift distributions for calculating the inversion of Limber's equation, hence we use the photometric and model estimates in the following sections.

### 7.2 Spatial correlation lengths

Taking each of the redshift distributions in turn, we have used the inverse of Limber's equation (Eq. 5) to calculate the correlation length,  $r_0$ , from the angular clustering amplitude of each of the samples. Setting  $\epsilon = \gamma - 3 = -1.2$  in Eq. 2 for the case of comoving clustering gives a comoving value of  $r_0$ . The correlation lengths are given in Table 2 and are plotted as a function of median redshift in Fig. 6 for each  $dN/dz$  (the plot excludes the IMPZ results for the faintest four samples, which are incomplete).

For the five brightest samples, corresponding to  $\langle z \rangle \lesssim 0.5$ , the correlation length varies slowly with redshift for each of the  $dN/dz$  distributions, but with an apparent dichotomy between the phenomenological models with  $r_0 \simeq 8 h^{-1} \text{ Mpc}$  and the IMPZ and GalICS estimates with  $r_0 \simeq 6 h^{-1} \text{ Mpc}$ . The uncertainty in the correlation length is dominated by this scatter between the  $dN/dz$

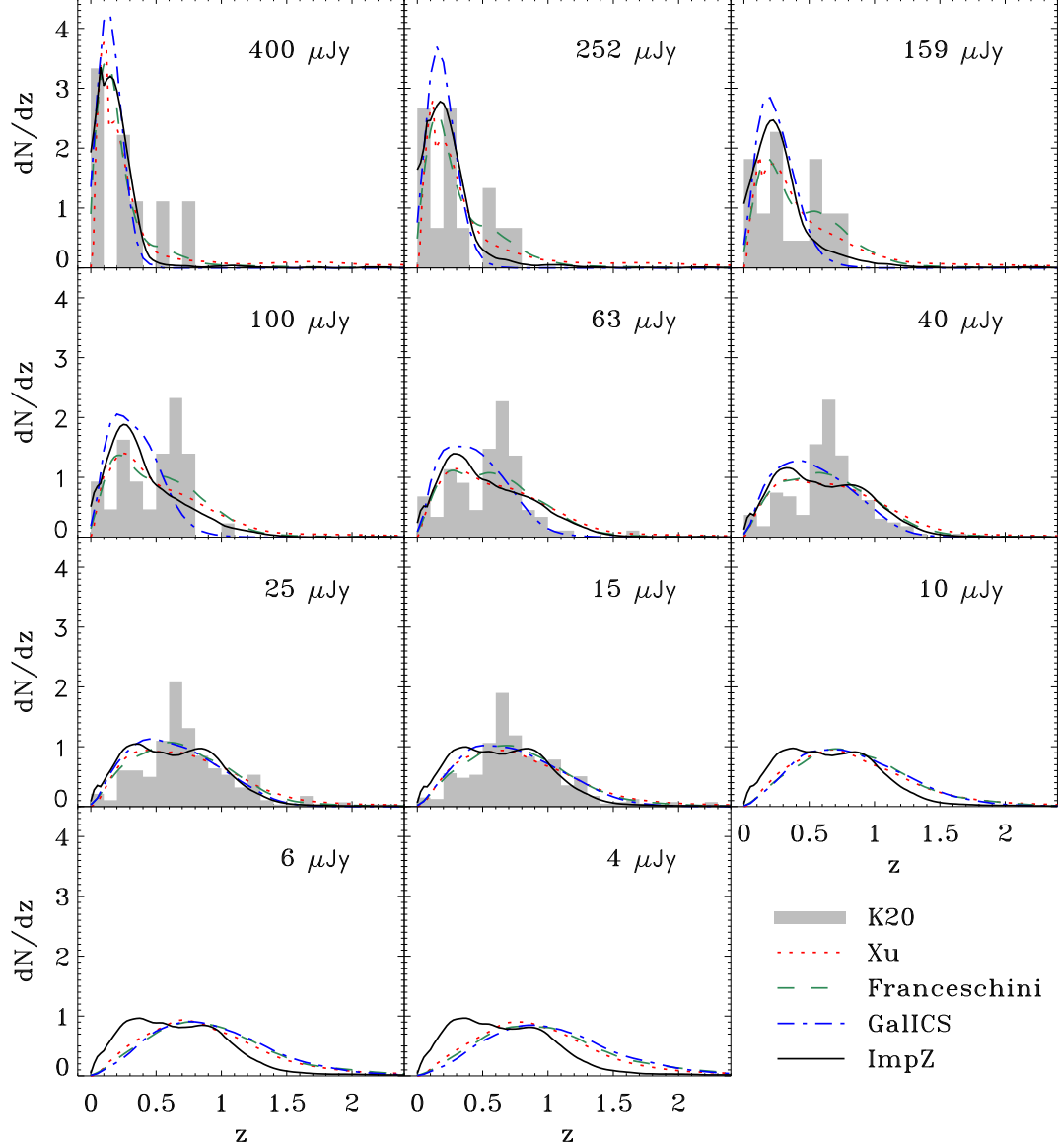


**Figure 5.** The redshift distributions for each of the SWIRE flux-limited samples derived from the phenomenological models of Xu et al. (2003) and Franceschini et al. (2006), the GalICS simulations (Hatton et al. 2003), and photometric redshifts from IMPZ (Babbedge et al. 2004). For comparison, the spectroscopic redshift distribution from the K20 survey (Mignoli et al. 2005) is shown in the grey histograms. Each distribution has been normalized over  $0 \leq z < 5$ .

estimates, not by the statistical uncertainty in measuring the angular clustering.

For all  $dN/dz$  distributions, the correlation length decreases rapidly with increasing redshift in the fainter samples (Fig. 6), falling from  $r_0 \simeq 6\text{--}8h^{-1}$  Mpc at  $z \simeq 0.5$  to  $3h^{-1}$  Mpc at  $z \simeq 1$ . Although the scatter in the median redshifts of the distributions are larger in these fainter samples, the average correlation lengths are more tightly constrained than those at lower redshift. (This is easily understood: the scatter between the median values of each redshift distribution is small compared with the actual widths of the

distributions, but at lower redshifts this is not the case.) If this high-redshift ( $z > 0.45$ ) evolution is fitted by an epsilon model (Eq. 2), we get best-fitting values of  $r_0 = 27 \pm 6h^{-1}$  Mpc and  $\epsilon = 4.8 \pm 0.8$  (Fig. 6, dotted line). This is very strong evolution, and implies that these sources are in environments that would evolve into massive clusters by  $z = 0$  (c.f. Fig. 9). Although we do not consider the epsilon model to be a realistic model of evolution to the present day, it does give some quantitative indication of the rapid change in clustering seen at these redshifts.

The spatial correlation lengths for the GalICS simulated cat-

**Table 4.** Average 3.6  $\mu\text{m}$  luminosities,  $\log_{10}(L_{3.6}/L_{\odot})$ , and redshifts,  $\langle z \rangle$ , for the Xu et al. (2003) and Franceschini et al. (2006) model redshift distributions.  $S_{36}$  are the flux limits ( $\mu\text{Jy}$ ).

$S_{36}$	$\langle z \rangle$	Xu et al.		Franceschini et al.	
		$\log_{10}(L_{3.6}/L_{\odot})$	$\langle z \rangle$	$\log_{10}(L_{3.6}/L_{\odot})$	$\langle z \rangle$
4.0	0.88	$9.45 \pm 0.48$	0.94	$9.24 \pm 0.55$	
6.3	0.84	$9.50 \pm 0.45$	0.88	$9.29 \pm 0.52$	
10.0	0.78	$9.57 \pm 0.42$	0.82	$9.39 \pm 0.50$	
15.9	0.74	$9.64 \pm 0.40$	0.74	$9.44 \pm 0.48$	
25.2	0.70	$9.72 \pm 0.39$	0.68	$9.54 \pm 0.45$	
40.0	0.66	$9.80 \pm 0.39$	0.62	$9.64 \pm 0.42$	
63.4	0.58	$9.87 \pm 0.40$	0.56	$9.64 \pm 0.43$	
100.5	0.46	$9.91 \pm 0.42$	0.48	$9.74 \pm 0.48$	
159.2	0.36	$9.91 \pm 0.45$	0.36	$9.84 \pm 0.47$	
252.4	0.26	$9.89 \pm 0.46$	0.24	$9.79 \pm 0.48$	
400.0	0.20	$9.84 \pm 0.43$	0.18	$9.64 \pm 0.50$	

alogues have been calculated in exactly the same way as those for the SWIRE observations. The amplitudes of the angular clustering (section 6) plus the redshift distributions (section 7.1) of the GalICS samples were used to calculate  $r_0$  through the inverse of Limber's equation (Eq. 5). These correlation lengths are also plotted in Fig. 6 (solid line, with the one-sigma errors in grey) for comparison with the results inferred from the observations. The GalICS simulations closely follow a stable clustering model, with a present-day correlation length of  $r_0 \simeq 6h^{-1}$  Mpc. As expected from the good agreement between the angular correlation functions of the SWIRE data and the GalICS simulations, the spatial correlation lengths from GalICS (grey region in Fig. 6) are consistent with those of SWIRE based on the GalICS redshift distributions (squares).

In Fig. 6, we see that the correlation lengths derived from the GalICS  $dN/dz$  (both the SWIRE values and the simulations) differ markedly from the results based on the models of Franceschini et al. (2006) and Xu et al. (2003). The latter predict that the SWIRE results are due to stronger clustering at low median redshifts, with rapid evolution at  $z \gtrsim 0.5$ , which is in contrast to the slowly evolving stable clustering derived from the GalICS simulations. The results based on the IMPZ photometric redshifts generally follow the GalICS data but are noticeably higher at  $z \simeq 0.5$ , suggesting more complex evolution than either the models or simulations predict. Given that the IMPZ redshift distributions are based on empirical data rather than models, we consider these results to be the best estimate of the true correlation lengths, adopting the GalICS results for samples fainter than  $S_{36} = 25 \mu\text{Jy}$  where the IMPZ data are incomplete. These correlation lengths are reproduced in Table 1 alongside the angular measurements.

So far we have interpreted the change in  $r_0$  as evolution in the clustering strength, but another possibility is that we are looking at different populations of sources in the different samples. For example, the fainter samples may be dominated by less massive galaxies which are located in halos of lower mass and so are intrinsically less clustered (e.g., Loveday et al. 1995; Norberg et al. 2002; Zehavi et al. 2005). We have investigated this possibility using the 3.6- $\mu\text{m}$  luminosity ( $L_{3.6}$ ) as a proxy for stellar mass. In Fig. 7 we plot the luminosity distributions of each sample from the Franceschini et al. (2006) and Xu et al. (2003) models, showing the contribution from early-type (elliptical/lenticular) and late-type (spiral, irregular, starburst) populations separately. For 3.6- $\mu\text{m}$  luminosities below  $10^{11} L_{\odot}$ , the two models predict very similar distributions for the total counts, but at higher luminosities the

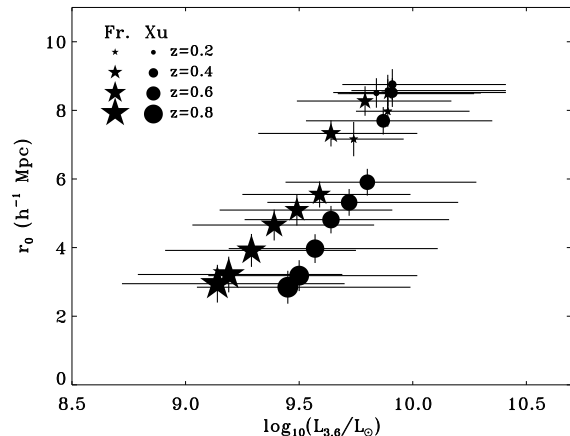


**Figure 8.** Correlation lengths,  $r_0$ , as a function of 3.6  $\mu\text{m}$  luminosity,  $\log_{10}(L_{3.6}/L_{\odot})$ , derived from the Franceschini et al. (2006, stars) and Xu et al. (2003, circles) model redshift distributions. The symbol size is proportional to the median redshift of each sample. Luminosity errors are the standard deviations of the luminosity distributions.

Xu et al. (2003) models have an extended tail of luminous late-type galaxies that are not present in the Franceschini et al. (2006) models. At bright flux limits ( $S_{36} \geq 40 \mu\text{Jy}$ ), the late-types are about 30–40 per cent of the total number of galaxies. The fraction of late-types then increases with decreasing flux limit, until in the faintest sample the late-types are 50 per cent of the total according to the Xu et al. (2003) model and 75 per cent of the total in the Franceschini et al. (2006) model. In all cases, the redshift distributions of the early-type galaxies are weighted towards higher redshifts than those of the late-type galaxies.

In Fig. 8 we plot the spatial correlation lengths against the average 3.6- $\mu\text{m}$  luminosities for the two models, and tabulate the luminosities in Tab. 4. For the brightest samples, i.e. the lowest median redshifts, the average luminosity is approximately constant, at  $\log_{10}(L_{3.6}/L_{\odot}) \simeq 9.8$ . At fainter flux limits ( $S_{36} = 40 \mu\text{Jy}$  and below), it is seen that there is a trend for  $r_0$  to decrease with decreasing average luminosity. Recalling that there is a progressively larger fraction of late-type galaxies as the flux limit decreases, both the decrease in average luminosity (mass) and the weaker clustering could be a consequence of the changing galaxy population – i.e. an increase in the number of lower-mass late-type galaxies. However, with the data we have available we cannot unambiguously disentangle evolution in the clustering strength from evolution in the relative populations of early-types and late-types.

Finally, we have compared the best estimates of the correlation lengths (Table 1) with values of  $r_0$  from the literature. This is shown in Fig. 9 where we plot  $r_0$  as a function of redshift for our data, together with a variety of galaxy and AGN correlation lengths, and several models, compiled by Farrah et al. (2006). The SWIRE sources are the most clustered population of galaxies at  $z < 1$ , with only clusters of galaxies exceeding the correlation lengths of the SWIRE samples. The solid lines are the halo models of Matarrese et al. (1997) which allow us to estimate the approximate masses of the halos that host the 3.6- $\mu\text{m}$  selected sources. At  $z \lesssim 0.5$  the inferred halo masses are approximately constant with redshift with  $\log(M_{\text{halo}}/M_{\odot}) \sim 13.5$ . The correlation lengths have been shown above to decrease with increasing redshift beyond  $z = 0.5$  and this corresponds to a decrease in halo mass from

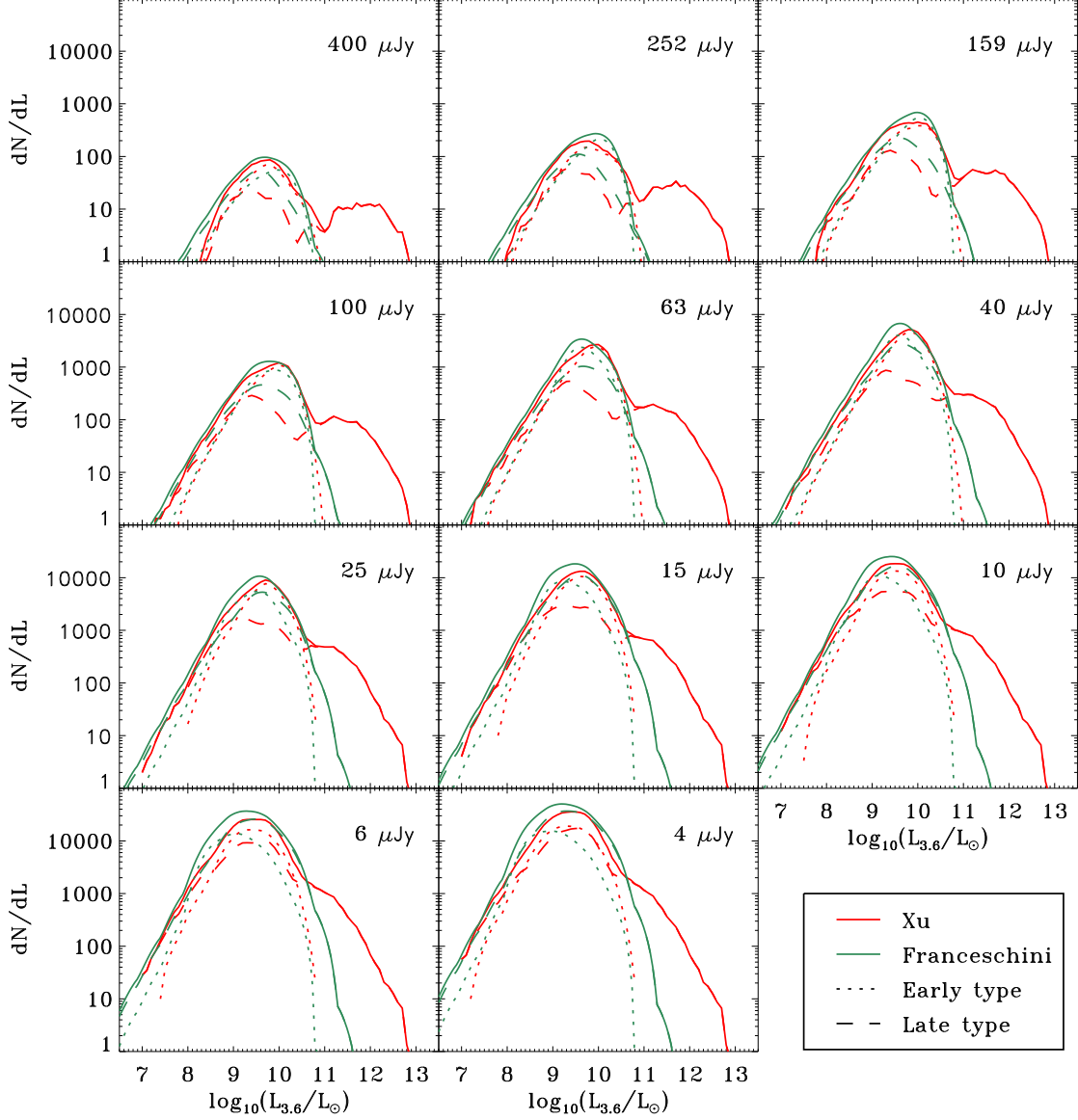


**Figure 7.** The distribution of 3.6  $\mu\text{m}$  luminosities for each of the eleven flux-limited samples from the Franceschini et al. (2006, green) and Xu et al. (2003, red) models.  $dN/dL$  is the number of sources per square degree per  $\log_{10} L_{3.6}$ . Dotted lines are the early types, dashed lines are the late types and solid lines are the total number of sources.

$10^{13.5} M_{\odot}$  to  $10^{12} M_{\odot}$  at  $z = 1$ . This is consistent with the idea that we are detecting more late-type galaxies, which have lower masses than the early-types that are prevalent in the brighter samples.

## 8 CONCLUSIONS

The SWIRE survey has allowed us to measure the angular clustering of sources selected at 3.6  $\mu\text{m}$  over larger scales and with greater

significance than previously has been possible. The two-point angular correlation function has been measured in eleven flux-limited samples down to  $S_{36} = 4 \mu\text{Jy}$ , corresponding to median redshifts  $z \leq 1$ . These angular results are in good agreement with the GALICS simulations and with  $K$ -band clustering measurements.

We have used Limber's equation to infer the spatial correlation lengths from the angular measurements and four estimates of the redshift distributions of each sample. We find that the systematic uncertainty in the  $dN/dz$  distribution dominates the statistical errors, and adopt the photometric redshift distribution from IMPZ

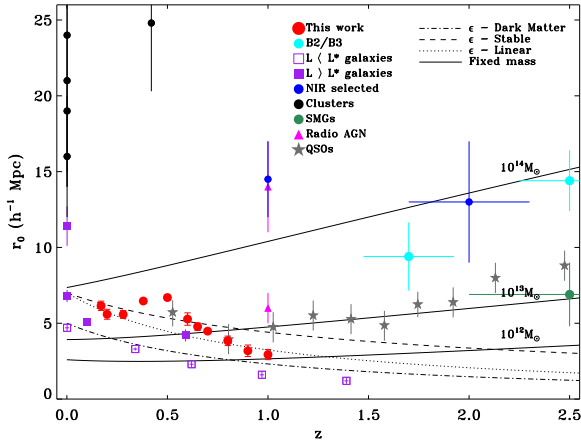


**Figure 9.** The best estimate of the comoving correlation length,  $r_0$ , of our samples (red circles) as a function of redshift, compared with values from the literature (Farrah et al. 2006, and references therein). The solid lines are the models of Matarrese et al. (1997) for halos of fixed mass, with masses as indicated. Also shown are indicative  $\epsilon$  models of clustering evolution: stable and linear models with  $r_0 = 7h^{-1}$  Mpc, corresponding to the average of our low- $z$  results; and a linear model normalized to the dark matter clustering strength,  $r_0 = 5h^{-1}$  Mpc, of Jenkins et al. (1998).

as the best estimate of  $dN/dz$ , extrapolating to higher redshifts using the GalICS results. The comoving correlation length varies slowly around  $r_0 = 6.1 \pm 0.5h^{-1}$  Mpc out to a median redshift of  $z = 0.5$  and then decreases with increasing redshift. If this change at higher redshifts is due to evolution in the clustering, then the required evolution is very strong (with  $r_0 = 27 \pm 6h^{-1}$  Mpc and  $\epsilon = 4.8 \pm 0.8$ ) and these SWIRE galaxies would be in environments that will evolve into massive clusters by the present day. There is some indication from the Franceschini et al. (2006) and Xu et al. (2003) phenomenological models that the change in correlation length is due to a decrease in the average 3.6- $\mu\text{m}$  luminosity (or equivalently, stellar mass) of the fainter samples rather than evolution in the clustering. This decrease in average luminosity is the result of an increased fraction of late-type galaxies in the faint samples. Comparing these SWIRE data with the halo models of Matarrese et al. (1997) suggests that the fainter samples are selecting sources in lower mass halos. These latter two results provide a consistent picture where lower-mass late-type galaxies are preferentially found in lower mass halos and thus have weaker clustering.

The comparison of our data with the GalICS simulations has shown that these models are a good match to the angular clustering, but their redshift distributions differ markedly from the phenomenological models and the photometric redshift distributions. This highlights the need for a better understanding of the spatial clustering and its evolution. Higher-resolution numerical models and improved semi-analytic models will allow us to directly explore the relation between the clustering of the galaxies and the dark matter, i.e. the bias. For example, the dark matter Millenium Simulation (Springel et al. 2005) has a lower mass resolution limit than GalICS, and combined with semi-analytic models of the galaxies it is a better match to the area and depth of SWIRE than the current models. Future work will explore the comparison between these models and the SWIRE data presented here.

## ACKNOWLEDGEMENTS

The pair-counting code NPT was provided by The Auton Lab at Carnegie Mellon University's School of Computer Science (<http://www.autonlab.org>) and we thank Andrew Moore et al. for making this software public. This work was funded by PPARC research grants to Seb Oliver. Support for this work, part of the *Spitzer* Space Telescope Legacy Science Programme, was provided by NASA through a contract issued by the Jet Propulsion Laboratory, California Institute of Technology under a contract with NASA.

## REFERENCES

- Babbedge, T. S. R., 2004, MNRAS, 353, 654
- Bardeen, J. M., Bond, J. R., Kaiser, N., Szalay, A. S. 1986, ApJ, 304, 15
- Baugh, C. M., Gardner, J. P., Frenk, C. S., Sharples, R. M. 1996, MNRAS, 283, L15
- Benson, A. J., Frenk, C. S., Baugh, C. M., Cole, S., Lacey, C. G. 2001, MNRAS, 327, 1041
- Berlind, A. A., Weinberg, D. H. 2002, ApJ, 575, 587
- Bertin, E., Arnouts, S., 1996, A&AS, 117, 393
- Blaizot, J., et al. 2006, MNRAS, 369, 1009
- Cimatti, A., et al. 2002, A&A, 392, 395
- Cole, S., Lacey, C. G., Baugh, C. M., Frenk, C. S. 2000, MNRAS, 319, 168
- Dye, S., et al., 2006, MNRAS, submitted, astro-ph/0603608
- Efstathiou, G., Bernstein, G., Katz, N., Tyson, J. A., Guhathakurta, P. 1991, ApJL, 380, L47
- Fang, F., et al. 2004, ApJS, 154, 35
- Farrah, D., et al. 2006, ApJL, 641, L17, and Erratum, 2006, ApJL, 643, L139
- Fazio, G. G., et al. 2004, ApJS, 154, 39
- Franceschini, A., et al. 2006, A&A, 453, 397
- Gonzalez-Solares, E., et al. 2004a, MNRAS, 352, 44
- Gonzalez-Solares, E., et al. 2004b, MNRAS, 358, 333
- Granato, G. L., Lacey, C. G., Silva, L., Bressan, A., Baugh, C. M., Cole, S., Frenk, C. S. 2000, ApJ, 542, 710
- Gray, A. G., Moore, A. W., Nichol, R. C., Connolly, A. J., Genovese, C., Wasserman, L. 2004, in F. Ochsenbein, M. Allen and D. Egret (eds), Astronomical Data Analysis Software and Systems XIII, ASP Conf Series, 314, 249
- Hatton, S., Devriendt, J. E. G., Ninin, S., Bouchet, F. R., Guiderdoni, B., & Vibert, D. 2003, MNRAS, 343, 75
- Jenkins, A., et al. 1998, ApJ, 499, 20
- Kaiser, N. 1984, ApJL, 284, L9
- Kong, X., et al. 2006, ApJ, 638, 72
- Kümmel, M. W., Wagner, S. J. 2000, A&A, 353, 867
- Landy, S. D., Szalay, A. S. 1993, ApJ, 412, 64
- Limber, D. N., 1953, ApJ, 117, 134
- Lonsdale, C. J., et al. 2003, PASP, 115, 897
- Lonsdale, C. J., et al. 2004, ApJS, 154, 54
- Loveday, J., Maddox, S. J., Efstathiou, G., Peterson, B. A. 1995, ApJL, 442, 457L
- Matarrese, S., Coles, P., Lucchin, F., Moscardini, L. 1997, MNRAS, 286, 115
- McCracken, H., Shanks, T., Metcalfe, N., Fong, R., Campos, A. 2000, MNRAS, 318, 913
- McMahon, R. G., Walton, N. A., Irwin, M. J., Lewis, J. R., Bunclark, P. S., Jones, D. H., 2001, New Astron. Rev., 45, 97

- Mignoli, M., et al. 2005, *A&A*, 437, 883
- Moscardini, L., Coles, P., Lucchin, F., Matarrese, S. 1998, *MNRAS*, 299, 95
- Norberg, P., et al. 2002, *MNRAS*, 332, 827
- Oliver, S. J., et al. 2000, *MNRAS*, 316, 749
- Oliver, S. J., et al. 2004, *ApJS*, 154, 30
- Overzier, R. A., Röttgering, H. J. A., Rengelink, R. B., Wilman, R. J., 2003, *A&A*, 405, 53
- Phillipps, S., Fong, R., Ellis, R. S., Fall, S. M., MacGillivray, H. T., 1978, *MNRAS*, 182, 673
- Pollo, A., et al. 2005, *A&A*, 439, 887
- Reike, G., et al. 2004, *ApJS*, 154, 25
- Roche, N., Eales, S., Hippelein, H., 1998, *MNRAS*, 295, 946
- Roche, N., Eales, S. A., Hippelein, H., Willott, C. J. 1999, *MNRAS*, 306, 538
- Roche, N., Almaini, O., Dunlop, J., Ivison, R. J., Willott, C. J. 2002, *MNRAS*, 337, 1282
- Roche, N., Dunlop, J. S., Almaini, O. 2003, *MNRAS*, 346, 803
- Rowan-Robinson, M., et al. 2004, *MNRAS*, 351, 1290
- Rowan-Robinson, M., et al. 2005, *AJ*, 129, 1183
- Scranton, R., et al. 2002, *ApJ*, 579, 48
- Skrutskie, M. F., et al. 2006, *AJ*, 131, 1163
- Springel, V., et al. 2005, *Nature*, 435, 629
- Surace, J. A., et al. 2005, ‘The SWIRE Data Release 2: Image Atlases and Source Catalogs for ELAIS-N1, ELAIS-N2, XMM-LSS and the Lockman Hole’, Spitzer Science Center, California Institute of Technology (Pasadena, CA)
- Surace, J. A., et al. 2006, *ApJS*, in preparation
- Werner, M., et al. 2004, *ApJS*, 154, 1
- Xu, C. K., Lonsdale, C. J., Shupe, D. L., Franceschini, A., Martin, C., Schiminovich, D. 2003, *ApJ*, 587, 90
- York, D. G., et al. 2000, *AJ*, 120, 1579
- Zehavi, I., et al. 2002, *ApJ*, 571, 172
- Zehavi, I., et al. 2005, *ApJ*, 621, 22

This paper has been typeset from a  $\text{\TeX}/\text{\LaTeX}$  file prepared by the author.